PHILOSOPHICAL TRANSACTIONS OF THE ROYAL SOCIETY A

rsta.royalsocietypublishing.org

Research

Cite this article: Zakri C, Blanc C, Grelet E, Zamora-Ledezma C, Puech N, Anglaret E, Poulin P. 2013 Liquid crystals of carbon nanotubes and graphene. Phil Trans R Soc A 371: 20120499.
http://dx.doi.org/10.1098/rsta.2012.0499

One contribution of 14 to a Theo Murphy Meeting Issue 'New frontiers in anisotropic fluid–particle composites'.

Subject Areas:
physical chemistry, materials science, nanotechnology

Keywords:
carbon nanotubes, graphene, liquid crystal, nematic, order parameter, organic electronics

Author for correspondence:
Philippe Poulin
e-mail: poulin@crpp-bordeaux.cnrs.fr

Liquid crystals of carbon nanotubes and graphene

Cécile Zakri[1,2], Christophe Blanc[3,4], Eric Grelet[1], Camilo Zamora-Ledezma[5], Nicolas Puech[1], Eric Anglaret[3,4] and Philippe Poulin[1]

[1]CNRS and [2]Université de Bordeaux, Centre de Recherche Paul Pascal (CRPP), UPR 8641, 33600 Pessac, France
[3]CNRS and [4]Université Montpellier 2, Laboratoire Charles Coulomb (LCC), UMR 5221, 34095 Montpellier, France
[5]Laboratorio de Física de la Materia Condensada, Centro de Física, Instituto Venezolano de Investigaciones Científicas, Altos de Pipe, 1024 Caracas, Venezuela

Liquid crystal ordering is an opportunity to develop novel materials and applications with spontaneously aligned nanotubes or graphene particles. Nevertheless, achieving high orientational order parameter and large monodomains remains a challenge. In addition, our restricted knowledge of the structure of the currently available materials is a limitation for fundamental studies and future applications. This paper presents recent methodologies that have been developed to achieve large monodomains of nematic liquid crystals. These allow quantification and increase of their order parameters. Nematic ordering provides an efficient way to prepare conductive films that exhibit anisotropic properties. In particular, it is shown how the electrical conductivity anisotropy increases with the order parameter of the nematic liquid crystal. The order parameter can be tuned by controlling the length and entanglement of the nanotubes. In the second part of the paper, recent results on graphene liquid crystals are reported. The possibility to obtain water-based liquid crystals stabilized by surfactant molecules is demonstrated. Structural and thermodynamic characterizations provide indirect but statistical information on the dimensions of the graphene flakes. From a general point of view, this work presents experimental approaches to optimize the use of nanocarbons as liquid crystals and provides new methodologies for the still challenging characterization of such materials.

1. Introduction

Carbon nanotubes (CNTs) and graphene are attracting a strong technological interest for applications in various fields from electronics to composites through biomedical applications. Development of suitable materials for such applications necessitates a fine control of the spatial ordering of the particles. A number of methods have been proposed over the past years to orient CNTs and graphene particles. These methods include, for example, field-induced alignment [1–4], shear-induced alignment, fibre processing and composite drawing [5–10], and dispersion in organized solvents [11–19]. Forming liquid crystals is one of the most appealing approaches. Indeed, a liquid crystal transition is a thermodynamic phenomenon that takes place spontaneously when anisotropic particles are suspended in a liquid medium at a sufficiently high concentration. Nematic liquid crystals exhibit orientational order but not positional order. This type of self-organized structure has been observed with CNTs [20–35] and more recently with graphene [36] or graphene oxide (GO) particles [37–41]. Nevertheless, several challenges are still faced in the use of nanocarbon-based liquid crystals in actual applications.

In particular, achieving large monodomains with high order parameter is an important issue. In most studies reported in the literature to date, CNT- and graphene-based liquid crystals exhibit only small monodomains and a number of topological defects. It is difficult in such conditions to quantitatively characterize and exploit their physical properties. Liquid crystals of true graphene flakes have only been achieved in superacids in the strict absence of moisture [36]. However, it would be preferable to have water-based liquid crystals in several situations, because water-based formulations can be more easily processed. Other groups instead used water-based solutions of GO flakes [40,41]. Graphene oxide is generally obtained by acid oxidation of graphite materials [42] and is water-soluble. But oxidation of graphene is known to severely downgrade the mechanical and electrical properties of the materials. Chemical reduction of GO to produce reduced graphene oxide (RGO) allows a partial restoration of the electronic conjugation and graphene properties. Unfortunately, this recovery is also associated with a gain in hydrophobicity with a loss of water solubility. This loss of water solubility hinders liquid crystal ordering in aqueous media. Lastly, the lack of bulk characterizations of the particles remains a significant challenge for the use of nanocarbon liquid crystals. Available CNTs or graphene dispersions are highly polydisperse in size and aspect ratio. Not knowing the average dimensions of the used particles is a critical limitation for their normalization and standardization in future technological developments. Characterizations via imaging techniques such as electron microscopy or atomic force microscopy (AFM) are often tedious and provide only results with limited statistics.

Considering the above challenges, in the present paper we describe recent research efforts towards the achievement of CNT liquid crystals that can be aligned on a large scale. This alignment allows the nematic order parameter to be measured and optimized to achieve a high degree of orientational order. The electrical properties of films made from CNT liquid crystals are characterized. The conductivity anisotropy is found to vary with the order parameter of the liquid crystal. The latter is controlled by changing the length and degree of entanglement of the CNTs. The experimental results are in good agreement with a simple model that takes into account the conducting paths in the nematic thin films. In the second part, we present the achievement of liquid crystals made of RGO particles. Thin films made from such particles are found to be significantly more conductive than films made from GO liquid crystals. In conclusion, we recall general features of liquid crystals made from nanocarbon particles and stress that the study of the liquid crystallinity of these materials is an indirect but particularly efficient approach to obtain quantitative information on the dimensions of the used particles and on their interactions. This new perspective suggests that fundamental studies of the liquid crystal behaviour of nanocarbons could contribute to the development of new methodologies for their standardization in future applications.

2. Order parameter and conductivity of highly aligned carbon nanotube liquid crystals

The degree of alignment of a nematic liquid crystal is usually quantified by a scalar called the orientational order parameter S. For three-dimensional systems, $S = \langle 3\cos^2\theta - 1\rangle/2$, where θ is the angle between the particle axis and the director, which is a unit vector that specifies the average alignment direction of the particles ($S = 0$ for an isotropic system and $S = 1$ for a perfect alignment). According to Onsager's predictions [43] for hard, rigid and infinitely long rods, S is expected to be 0.79 at the isotropic–nematic transition. Unfortunately, it is often difficult to measure the order parameter of CNT liquid crystals, because the materials often exhibit a high density of topological defects [28,31]. Nanotubes stabilized in water by single-stranded DNA molecules can exhibit nematic ordering with a phase diagram consistent with Onsager's prediction [23]. Such liquid crystals could be oriented over large monodomains through shear-induced alignment procedures, thereby offering the opportunity to measure the nematic order parameter S [28]. However, in spite of phase boundaries consistent with Onsager's predictions, the values of the order parameter S measured by polarized micro-Raman spectroscopy of aligned films was much smaller than expected [28].

The origin of this surprising observation remained unclear until recently. Lu & Chen [27] demonstrated that impurities could greatly hinder the ordering of nanotubes in concentrated suspensions. Nevertheless, nanotubes of relatively high purity were also used in other studies [28,31] and could not lead to materials aligned on the macroscopic scale. Song & Windle [31] have shown that the morphology of the nanotubes can affect the texture of nematic liquid crystals and the density of topological defects. In particular, the authors have demonstrated that long nanotubes could be bent around the core of topological defects. The stabilization of topological defects by deformed and not perfectly straight nanotubes could explain the difficulty in aligning such materials over large monodomains. Even shear-aligned and dried materials could indeed still contain defects at the microscopic scale, which can neither be visualized by optical microscopy nor detected by polarized Raman spectroscopy. Indeed, optical microscopy, as well as other optical or scattering techniques, is generally efficient at analysing surface areas of a few micrometres square. Topological defects can be stabilized by long and wavy nanotubes, and artificially yield low order parameters. Long and/or wavy nanotubes can also increase the viscosity of the material and even yield some elastic behaviour. Elasticity of the materials and the presence of a yield stress can hinder flow of the material and the spontaneous coarsening of topological defects.

In order to clarify these issues and attempt to obtain highly aligned liquid crystals, we investigated the behaviour of CNTs that were shortened and disentangled by high-power sonication [44–46], and stabilized by bile salt (BS) molecules. BSs have already been shown to be excellent dispersants for CNTs [47]. They comprise sodium cholate and sodium deoxycholate salts with the chemical structures given, for example, in Wenseleers *et al*. [47]. The molecules include a hydrophobic part made of cyclic aliphatic groups and a charged ionic polar head. This structure provides an amphiphilic behaviour to the molecules and the capability to stabilize hydrophobic particles in water.

Shortened nanotubes can in addition be sorted by centrifugation [48]. Liquid crystals are obtained by dispersing sorted nanotubes in water. The details of the materials preparation are given in Puech *et al*. [33]. Nevertheless, the main points are recalled here. The starting CNT material is a 'wet cake'-like material made of purified CNTs. It was provided by Thomas Swan (UK) under the trade name Elicarb (batch number K3778). The CNTs are assembled in the 'wet cake' as bundles and entangled aggregates. The term 'wet cake' means that the samples contain a certain fraction of water, but are still in a solid form. 'Wet cakes' are obtained by keeping a small amount of water after purification of the materials. Such materials are used because they can be more easily dispersed in an aqueous medium than nanotubes that have been purified and then fully dried. Full drying leads to the bundling and aggregation of nanotubes via strong van

der Waals interactions. CNTs in the form of wet cakes are suspended and diluted in aqueous solutions of BSs. The dispersions are homogenized by sonication. All the sonication experiments were performed in 10 cm^3 aqueous solutions that contain 0.5 wt% CNTs and 0.5 wt% of BS. The homogeneity of the dispersions was checked at the micro-scale by optical microscopy. BS dispersants allow an effective debundling of the nanotubes. The dispersants produce repulsive interactions that prevent the nanotubes from re-forming bundles.

Debundling of the CNTs at smaller scales was also monitored and confirmed by the observation of photoluminescence [33]. Starting with low concentrations allows homogeneous dispersions to be easily achieved. However, in agreement with Onsager's model, the systems do not form liquid crystals at low concentration. The samples have to be concentrated using ultracentrifugation. Long CNTs settle faster than short particles at the bottom of the vials during ultracentrifugation. This effect offers, therefore, an opportunity to sort nanotubes by their length. After the sonication treatments, the biggest aggregates and large bundles are removed via a gentle centrifugation at 2700g for 30 min. The supernatant is then collected and ultracentrifuged at 210 000g for various durations from 30 min to 3 h at room temperature. Ultracentrifugation allows the concentration of the nanotubes at the bottom of the vial to be increased. Nematic phases are obtained in these conditions. The concentrated sediments (nanotube fraction typically above 5 wt% as measured by thermogravimetric analysis) are separated from the remaining supernatants and homogenized by vigorous mixing.

A concentrated system forms a monophasic nematic liquid crystal as shown by optical microscopy [33]. Macroscopic alignment can be achieved by shear-induced alignment. A droplet of liquid crystal is sandwiched between two glass slides and sheared by moving the upper slide as already shown in Zamora-Ledezma *et al.* [28]. The upper slide is removed to allow the quick drying of the thin film as water evaporates. The film thickness after drying was measured by both AFM and surface profilometry (Veeco Dektak 3). It was found that the thickness of dried films varied from 0.1 to 0.5 µm depending on the samples. As reported in a previous study of similar materials [28,33], the order parameter of the samples does not evolve during drying. This was checked by comparing samples in open cells to samples in cells that were sealed with glue immediately after shear to avoid water evaporation. It is believed that the absence of any difference arises from the high viscosity of the materials and from the fast rate of drying. The time taken for drying is too short to allow substantial structural changes.

We investigated materials at, or close to, the isotropic–nematic transition, in order to achieve comparisons of order parameters in similar thermodynamic conditions. While the phase boundaries have not been determined accurately in this work for all the samples, it was observed that the systems were in monophasic isotropic states for nanotube weight fractions typically below 3 wt%, and in monophasic nematic states for nanotube weight fractions typically above 5 wt%. Isotropic–nematic equilibrium was observed in between those boundaries. We stress that previous studies of the phase diagrams of CNT liquid crystals allowed the aspect ratio of the CNT to be evaluated [22]. Theory [43,49] predicts that monodisperse and rigid rods of diameter D and length L form an isotropic phase for a volume fraction lower than $\phi I_{\mathrm{the}} = 3.3\,D/L$ and a nematic phase above a volume fraction $\phi N_{\mathrm{the}} = 4.5\,D/L$ (ϕI_{the} and ϕN_{the} are the volume fractions of the phase boundaries theoretically expected). In between these boundaries, coexistence between a nematic and isotropic phase is expected. The ratio $\phi N_{\mathrm{the}}/\phi I_{\mathrm{the}}$ is 1.4. In the experiments reported in Zakri & Poulin [22], the authors found a ratio of $\phi N/\phi I = 2$ (ϕI and ϕN are the volume fractions of the phase boundaries experimentally observed). This experimental value is greater than 1.4, the value theoretically expected for monodisperse rod-like particles. The discrepancy between experiments and theory was ascribed to the polydispersity of the samples. Nevertheless, the phase boundaries were still consistent with the aspect ratio estimated from light scattering experiments and electron microscopy observations.

Transmission electron microscopy (TEM) was also used to qualitatively observe the effect of sonication and ultracentrifugation for different CNT suspensions stabilized by BS molecules (figure 1). The suspensions have been prepared at two different sonication times t_{US} and ultracentrifugation times t_{UC}. It is difficult to provide a reliable statistical analysis of the TEM

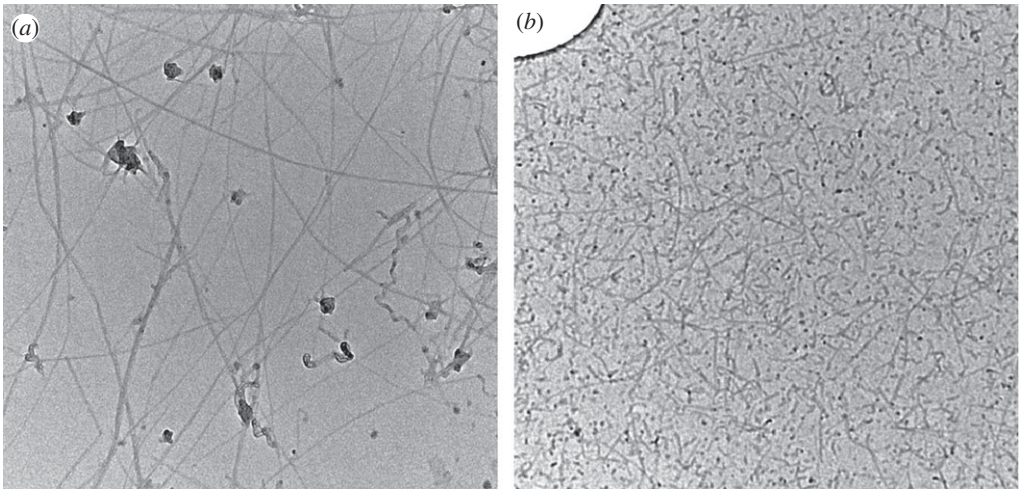

Figure 1. Transmission electron microscopy of CNTs after (*a*) 30 min of sonication and 45 min of ultracentrifugation at 210 000*g*, and (*b*) 3 h of sonication and 3 h of ultracentrifugation at 210 000*g*. *Scale*: the image size is 1.5 × 1.5 μm.

images, because only a few nanotubes can be observed on each picture. Nevertheless, the present TEM images demonstrate that the length and the diameter of CNTs clearly decrease for long sonication and ultracentrifugation times. Branched nanotubes and kinks of long nanotubes can be seen in weakly sonicated materials (figure 1*a*). By contrast, shorter nanotubes appear to be straighter (figure 1*b*).

Deeper characterizations of CNT liquid crystals have been performed using polarized Raman spectroscopy [28,33]. The order parameter S was deduced from Raman measurements carried out using the laser line at 1064 nm (1.16 eV) of a Nd : YAG laser and a Fourier transform (Bruker RFS100) spectrometer. Spectra were measured in three different polarization configurations, VV, VH and HH, where V or H correspond to polarizations of the incident and scattered waves parallel or perpendicular to the alignment direction. The spectra exhibit different peaks typical for CNTs. In particular they exhibit the so-called G band at a Raman shift of approximately 1600 cm^{-1}. The value of S is directly computed from a function of the G-band intensities I_{VV}, I_{VH} and I_{HH} in the above polarization configurations. The relation between S and the scattered intensities as well as possible corrections for dichroism can be found in recent studies [28,33].

The orientational order parameter was measured as a function of the sonication and centrifugation treatments of the CNT dispersions. The value of the order parameter S as a function of the nanotube sonication time t_{US} is reported in figure 2*a*. Films made from liquid crystals of long CNTs exhibit a small order parameter ($S \approx 0.3$). This can be understood by the presence of defects, kinks and junctions of the longest CNTs. All these structural features can induce orientational disorder. This is schematically sketched in the left inset of figure 2*a*. By contrast, the right inset shows improved alignment of shortened nanotubes that have been sonicated and sorted by ultracentrifugation. The high viscosity of samples containing long CNTs can also explain the difficulty in aligning the materials. Considering these possible limitations, the order parameter is expected to be improved by selecting shortened and individualized nanotubes. These tubes are straighter and can exhibit a greater level of alignment.

The value of S as a function of the ultracentrifugation time t_{UC} is shown in figure 2*b*. Each sample has been sonicated for 2 h. For the first sample at $t_{UC} = 30$ min, no ordering could be detected via optical microscopy under crossed polarizers. After a longer ultracentrifugation time, the nematic order appears and increases strongly until a constant regime is reached at about $t_{UC} =$ 2 h. This result indicates that nematic ordering is mostly hindered by long CNTs that sediment at short times. In view of this, we prepared a sample by performing an additional 45 min long

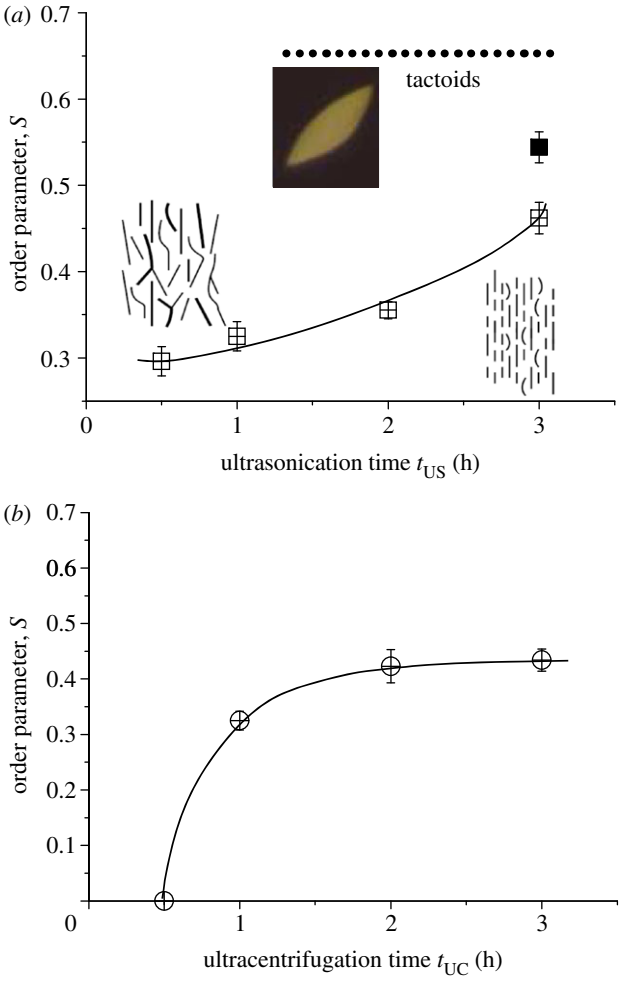

Figure 2. (*a*) Order parameter of nematic dried films made with CNT dispersions that have been sonicated during different times t_{US}. All the used dispersions have undergone a single ultracentrifugation step for 1 h at 210 000*g*. The black square shows the order parameter of a sample that has undergone a supplementary ultracentrifugation step for 45 min. The left schematic shows the poor ordering in weakly sonicated nanotubes. Some branched nanotubes and wavy ones with kinks can act as disordering species. Improvement of alignment, as sketched in the right schematic, is brought about by sonication-induced shortening and nanotube sorting by ultracentrifugation. The dotted line at the top of the graph shows the order parameter measured in tactoids $S \sim 0.65$. An optical micrograph of a tactoid observed in between crossed polarizers is shown below the dotted line. The length (longer axis) of the tactoid shown is about 10 µm. (*b*) Order parameter of nematic dried films made with CNT dispersions that have been ultracentrifuged during different times t_{UC}. All the used dispersions have been sonicated for 2 h. (Online version in colour.)

ultracentrifugation step immediately after sonication ($t_{US} = 3$ h) to remove the longest and wavy nanotubes. The sample was then treated as the other investigated samples. The orientational order of this material is greatly improved. Indeed, as shown in figure 2*a*, *S* is increased up to 0.55.

The isotropic–nematic phase transition can also be used to sort nanotubes by fractionation effects. Indeed, the nematic phase is expected to be enriched with the straighter nanotubes that exhibit the greatest aspect ratio. This offers an additional opportunity to select nanotubes for achieving more ordered nematics. Samples are prepared in the nematic–isotropic two-phase region by diluting a nematic sample in an appropriate volume of aqueous BS solution. Small spindle-like droplets are observed when the isotropic phase is in large excess. These droplets can

be observed by optical microscopy with the materials sandwiched in between a glass slide and a coverslip. They are reminiscent of nematic tactoids (figure 2*a*) [34,50] found in dispersions of highly anisometric colloidal particles. A tactoid is a particle that has a spindle shape and can be observed using polarized microscopy. Under crossed polarizers, the present tactoids can be uniformly 'extinct' depending on their orientation relative to the polarizers [34]. In contrast to the bulk nematic phase, this observation shows the spontaneous and uniform alignment of the nanotubes with a total absence of heterogeneities in the bulk nematic phase. The nanotubes are uniformly oriented along the main axis of the spindles. The present tactoids are ideal candidates for measuring the order parameter of a nanotube liquid crystal in the absence of heterogeneities. Indeed, tactoids can be several micrometres in length and diameter. Quantitative analyses are performed by using glass cells that have a thickness of 10 µm. The cells are filled by capillarity with diluted solutions that lie in the biphasic isotropic–nematic region with a large excess of isotropic phase. No shear was applied. The tactoids are examined in micro-Raman experiments with an incident beam diameter focused into a 10 µm diameter spot. Care is taken to analyse only droplets larger than the beam size. This procedure also ensures that the tactoids occupy the whole thickness of the cell. The order parameter measured for tactoids obtained with dispersions achieved for $t_{US} = 3$ h and $t_{UC} = 2$ h is $S = 0.65$ (figure 2*a*). This value is greater than the one observed for bulk materials. It approaches the value theoretically expected for ideal hard rods.

Packing and aligning CNTs on a large scale are routes towards the optimized manifestation of their intrinsic axial properties in a macroscopic film. Conductivity anisotropy has been experimentally observed in a number of aligned CNT materials, but a quantitative relationship between the conductivity anisotropy and the degree of ordering has yet to be determined. This relationship is expected to be relevant for a variety of materials, from rigid conducting polymers to metal nanowires and CNTs. The above possibility to tune the order parameter of CNT liquid crystal allows us to experimentally determine this relationship. Different thin films made from more or less ordered liquid crystals are prepared. The CNT concentration in the nematic phase is typically a few weight per cent. Considering, for example, a value of 5 wt%, the weight fraction of solid content is expected to be multiplied by a factor of 20 during drying. Water evaporation results, therefore, in a strong decrease of the film thickness and in the quasi-two-dimensional confinement of the nanotubes. The sheared and dried films are thinner than the average nanotube length.

Considering the present confinement conditions, it is assumed that the contribution of nanotubes pointing out of the plane can be neglected in the estimation of the order parameter. The degree of ordering is quantitatively characterized by polarized Raman spectroscopy [35] following the experimental procedure described above. In two dimensions, the scalar order parameter is given by

$$S = \langle 2\cos^2\theta - 1 \rangle. \tag{2.1}$$

The samples are kept at 80°C under vacuum for 24 h prior to each measurement in order to avoid artefacts due to the presence of moisture.

The conductivity of the present nanotube assemblies is limited by the resistivity of the intertube contacts. Net values of the surface resistivity typically range from 10^3 to 10^4 Ω per square for the investigated samples. These values depend on the nanotube features' including length, aspect ratio, electronic properties and remaining surfactant molecules at the CNT interfaces. In particular, surfactant molecules at the nanotube interfaces are expected to increase the contact resistance between neighbouring nanotubes. By contrast, the surface conductivity anisotropy defined as the ratio between the surface conductivity parallel to and perpendicular to the nematic director $\sigma_{ani} = \sigma_{\parallel}/\sigma_{\perp}$ does not depend on such features. This ratio is expected to depend only on the ordering and anisotropy of the nanotube assembly. As shown in figure 3, it is actually observed that σ_{ani} increases with the order parameter. The ratio σ_{ani} is close to 1 for films that are weakly ordered. It increases up to $\sigma_{ani} \sim 8$ for the more ordered nematics with an order parameter $S \sim 0.6$. Fischer *et al*. [51] modelled magnetically aligned CNT films as an ensemble of one-dimensional conducting paths in the plane of the sample. Each path contains on

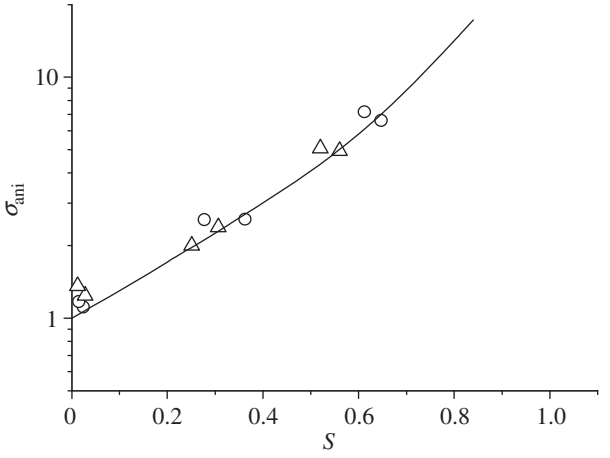

Figure 3. Surface conductivity anisotropy as a function of the order parameter. Circles and triangles, respectively, correspond to samples sonicated for 30 and 180 min. The continuous curve corresponds to the anisotropy calculated from equation (2.2) for an ordered assembly of conducting rods without any fitting parameter and with a two-dimensional Gaussian distribution of their orientation with respect to the nematic director (see text).

average n particles of fixed length. Consequently the resistance of each path is proportional to n (conductance proportional to $1/n$). This model considers that the electric current is limited by the intrinsic resistivity of the nanotubes. Intertube contacts are in the present case more resistive than nanotubes. Indeed, the junction resistance for single-wall CNTs is about 200–400 kΩ [52,53]. The presently investigated nanotubes are short (length $< 1\,\mu$m) and their resistivity is expected to be only a few kiloohms [52,54]. This is why the junction resistances have to be taken into account to estimate the conductivity.

Evaluating the number of intertube contacts or evaluating the number of nanotubes is equivalent as long as one-dimensional paths are considered. For a given total number of particles N, the number of paths is N/n. Assuming that the conducting paths are in parallel in a given direction, the conductance of the ensemble is directly proportional to N/n times $1/n$. The resistance is, therefore, expected to scale as n^2. The average number of particles required to connect edges of the film differs along the vertical and horizontal directions because of the CNT alignment. This average number is proportional to the projection length of the nanotubes on the considered axes of the film. The resultant conductivity anisotropy is expected to be

$$\sigma_{\text{ani-cal}} = \left[\frac{\langle \cos\theta \rangle}{\langle |\sin\theta| \rangle}\right]^2. \tag{2.2}$$

Unfortunately, this relationship could not be systematically tested as a function of S by Fischer *et al.* [51] because the anisotropy predicted from Raman scattering measurements was almost the same for the two samples investigated by the authors.

More recently, Lu & Chen [27] achieved a macroscopically aligned conductive film from a CNT liquid crystal. The authors estimated from electron micrographs an order parameter of about 0.9 for this film. The surface conductivity anisotropy was about 18. Unfortunately, this value does not yet allow a full comparison with the proposed model since it is obtained for a single system.

Taking advantage of the present Raman spectroscopy characterizations and of the possibility to vary the order parameter of the films, a systematic analysis of the conductivity anisotropy can be proposed [35]. Estimation of the surface conductivity in equation (2.2) necessitates the definition of a distribution for the θ angle. It is assumed that the CNTs lie in the plane of the substrate and are distributed in two dimensions with a Gaussian distribution of their orientation $p(\theta) = (a/\sqrt{2\pi\sigma^2})\mathrm{e}^{-\theta^2/2\sigma^2}$, with $\int_{-\pi/2}^{\pi/2} p(\theta)\,\mathrm{d}\theta = 1$. Averaging of the number of conducting paths along

different directions in equation (2.2) can then be achieved using Gaussian distributions associated with different order parameters. This method allows the surface conductivity anisotropy to be computed as a function of S without any fitting parameter. The results shown in figure 3 show a good agreement of the computed and experimental data. This good agreement corroborates that the present approach captures the main physical mechanisms involved. Nevertheless, the model remains particularly simple and questionable. Tests with other types of conducting rods would be useful to confirm the validity and generality of the present results.

3. Liquid crystals of reduced graphene oxide

We report an approach that allows the formation of aqueous lyotropic liquid crystals using RGO in spite of their lack of water solubility [41]. The objective is to combine the physical properties of RGO materials and the easy processing of GO flakes. In this approach, the RGO particles are stabilized by BSs that act as surfactants. Surfactant-stabilized RGO, in contrast to neat RGO, can form liquid crystals in water. We note that, in contrast to GO flakes, these colloidal particles are metastable. From a thermodynamic point of view, the behaviour of surfactant-stabilized RGO is similar to the behaviour of surfactant-stabilized colloids or emulsions. The details of the materials preparations are available in Zamora-Ledezma *et al*. [41]. Nevertheless, some important features distinct from the processes used in the already reported methods are recalled in the present paper.

Expanded graphite (EG) is used as the source material. EG is a commercially available product obtained from natural graphite that has been immersed in chromic and sulfuric acids and thermally treated to expand crystal lattice planes apart, thus expanding graphite. Graphene oxide is obtained by following the so-called modified Hummers method [42,55]. This method involves two oxidation stages. The first oxidation is achieved in the presence of $K_2S_2O_8$ and P_2O_5 in a concentrated aqueous solution of H_2SO_4. For the second oxidation process, the materials collected after the first oxidation are re-suspended in a concentrated aqueous solution of H_2SO_4 into which $KMnO_4$ is slowly added. The reaction is completed by adding a mixture of water and H_2O_2. The colour of the sample after this oxidation process is brown-orange. The obtained particles are water-soluble and do not form any aggregates visible by optical microscopy, as shown in figure 4*a*. GO forms true thermodynamically stable solutions. As indicated above, several groups have already reported the attainment of liquid crystals using GO flakes in water. Unfortunately, the mechanical and electronic properties of graphene are severely downgraded by chemical oxidation. Various methods can be used to reduce GO into RGO. Chemical reduction using hydrazine is known, for example, to be efficient at restoring, at least partially, electronic conjugation and conductivity. However, chemical reduction is associated with a gain in hydrophobicity, which makes RGO insoluble in water and, therefore, not directly suitable to achieve liquid crystals. But following the strategy already used for CNTs, we use BS surfactants to stabilize RGO flakes and achieve liquid crystals.

Surfactant-stabilized RGO (RGO-BS) is achieved by first diluting the GO particles in an aqueous solution of BSs instead of pure water. The BS weight fraction is 0.5 wt%. This fraction is kept constant for all the samples. In all the following steps, surfactant-stabilized systems of RGO are achieved by using aqueous solutions of BSs instead of pure water. The chemical reduction is achieved following the method described in Li *et al*. [55], except that surfactant is present during the reduction. The presence of surfactant is a key difference from previous studies, because the graphene flakes do not aggregate during the chemical reduction, as is usually observed in aqueous media. The colour of the sample becomes black during the reaction. This confirms the chemical reduction of the flakes. But no aggregates can be observed, thereby confirming the efficiency of the BSs at maintaining the RGO flakes individually suspended in solution. The above suspensions (GO in water and RGO in BS/water) are ultracentrifuged for 60 min in order to obtain lyotropic liquid crystal phases [41]. Concentrated sediments are obtained at the bottom of the vials. They are then diluted by adding a controlled amount of solvent. The obtained samples are characterized by optical microscopy and small-angle X-ray scattering (SAXS). For X-ray

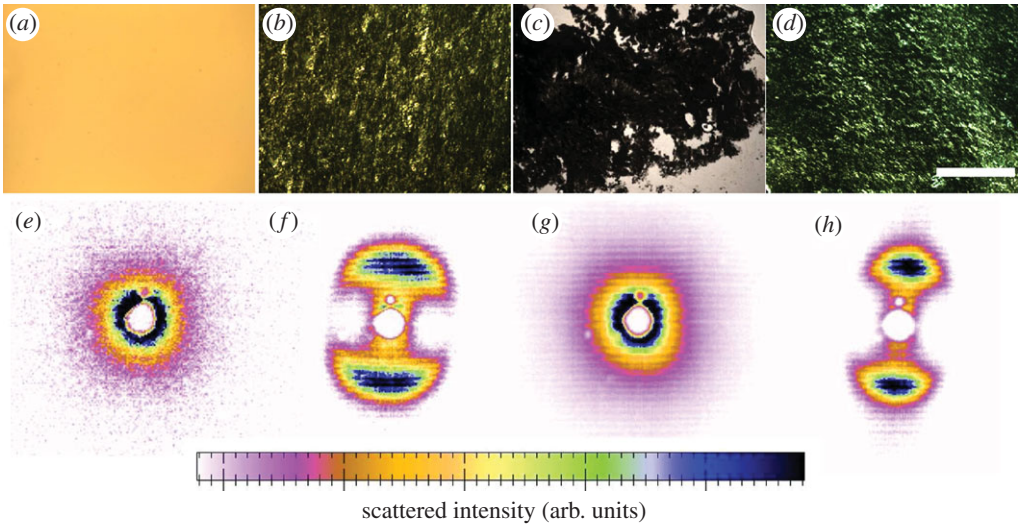

Figure 4. (*a*) Optical micrograph of an isotropic suspension of diluted GO. (*b*,*d*) Optical micrographs between crossed polarizers for concentrated GO (*b*) and RGO-BS (*d*) suspensions after a single ultracentrifugation at 210 000*g* for 60 min. The axes of the crossed polarizers are in horizontal and vertical directions. (*c*) Optical micrograph of RGO in the absence of BS surfactant: the particles are unstable and form aggregates. The scale bar shown in (*d*) is 400 μm and is the same for all the pictures. (*e*–*h*) Corresponding SAXS two-dimensional patterns for all graphene aqueous suspensions shown in the first row. The graphene concentrations are from left to right: 0.1, 6.6, 5 and 5.9 wt%. The materials in (*f*) and (*h*) exhibit 'butterfly' patterns arising from nematic ordering. The patterns are slightly shifted with respect to the horizontal axis. This observation reflects a macroscopic alignment of the director with a small tilt with respect to the capillary tube. Adapted from Zamora-Ledezma *et al*. [41]. (Online version in colour.)

measurements, cylindrical quartz capillary tubes of 0.5 mm diameter are filled with isotropic dispersions and nematic phases. The capillaries are centrifuged at 2700*g* for 1 min to let the viscous sample settle at the bottom of the tubes.

The liquid crystallinity of the materials is first assessed by optical microscopy using crossed polarizers. As shown in figure 4*b*,*d*, birefringence and typical nematic textures are observed for concentrated GO and RGO-BS materials. We note that the nematic textures do not look like the textures of thermotropic molecular liquid crystals, but are instead reminiscent of particle-based liquid crystals. Those nematics are not aligned on a macroscopic scale and exhibit only small disoriented monodomains. The graphene concentrations for these samples are 6.6 wt% and 5.9 wt%, respectively. Highly diluted systems are isotropic. The RGO suspension in the absence of BS was found to be unstable, as shown in figure 4*c*, and does not exhibit any phase transition towards a liquid crystalline state. The dispersions form a single nematic phase above a weight fraction of approximately 1.5 wt% for both GO and RGO-BS materials. A biphasic region is observed between 1.0 and 1.5 wt%. The materials form a single isotropic phase at lower weight fractions. Assuming a material density of 1.8 g cm^{-3} [56], a weight fraction of 1.0 wt% corresponds to a volume fraction of about 0.6 per cent for the clearing point of the nematic phase.

According to theoretical predictions [57,58] the isotropic–nematic transition of thin platelets occurs at a volume fraction of approximately $4\delta/D$, where δ is the layer thickness and D is the diameter of the platelets. This value is approximate for monodisperse platelets. For monodisperse systems, the width of the biphasic region is relatively narrow [57,58]. Even if this width is not accurately determined in the present work, it seems to be greater than that expected for monodisperse platelets. This phenomenon can presumably be ascribed to the polydispersity of the GO and RGO flakes. Nevertheless, assuming a monodisperse distribution, it is still possible to deduce from the above theoretical expectations that the average aspect ratios δ/D of GO and RGO particles are similar and are about 1.5×10^{-3}.

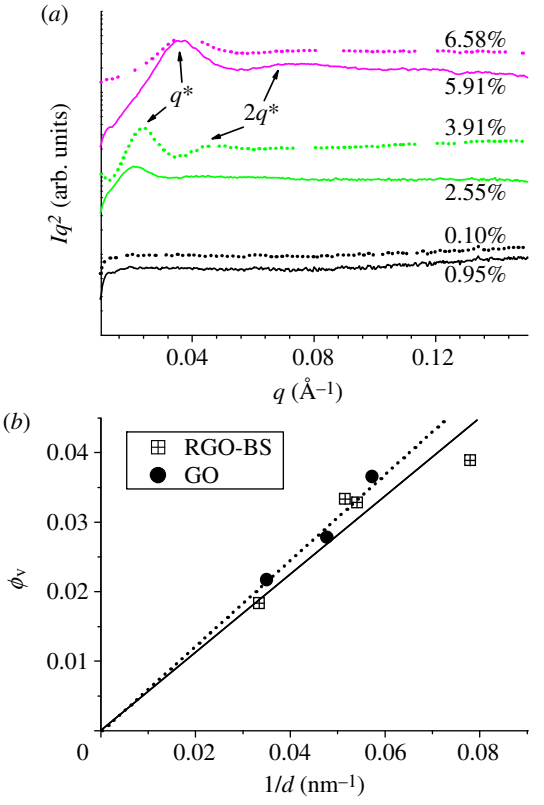

Figure 5. (*a*) SAXS spectra depicting the scattered intensity as a function of the scattering wavevector q for suspensions of RGO + BS (full line) and GO (dotted line) at different concentrations. The weight fractions are given next to each curve. (*b*) Volume fraction ϕ_v of the different GO and RGO-BS nematic phases as a function of the inverse of their characteristic distance $1/d$. The lines are linear fits, with a dotted line for GO and a continuous line for RGO-BS materials. (Online version in colour.)

The aqueous nematic phases of GO and RGO are further investigated by SAXS. A series of samples with different weight fractions of graphene materials is prepared by diluting the samples obtained after ultracentrifugation. Typical two-dimensional diffraction patterns are shown in figure 4*e–h*. As expected for the isotropic suspension, the pattern in figure 4*e* reflects the absence of pronounced structural ordering. As shown in figure 4*g*, a similar result is found for the concentrated RGO suspension in the absence of BS. By contrast the scattered intensities in figure 4*f,h* for the GO and RGO-BS stable dispersions exhibit typical 'butterfly' anisotropic patterns. The large radial width of this anisotropic pattern reflects a liquid-like order, typical of a nematic organization. It also surprisingly reflects a macroscopic alignment of the director field of the nematic phases with a small tilt with respect to the capillary axis. This macroscopic ordering is ascribed to the shear-induced alignment and centrifugal forces during centrifugation to fill the capillaries.

The present behaviour suggests that graphene and GO liquid crystals can be easily aligned in spite of the large size and aspect ratio of the flakes. The radial width of the integrated scattered intensity I multiplied by the square of the wavevector q as a function of q is shown in figure 5*a* (Kratky plot) for the GO and RGO-BS liquid crystals at different concentrations. The multiplication by q^2 should provide a flat baseline for scatterers with a plate-like structure. Indeed, the form factor of plate-like particles averaged over all possible orientations is expected to scale as q^{-2}. Peaks at q^* arising from the diffraction of the ordered flakes are clearly observed. These peaks reflect single layer exfoliation of the GO or RGO flakes. The present nematics are made of highly polydisperse disc-like particles. In contrast to conventional columnar liquid

crystals made of monodisperse discs, the present materials can be more likely described as a pseudo-lamellar structure. This is supported by the observation of peaks at q^* and $2q^*$ in the spectra of some samples for the first- and second-order diffraction peaks. The quasi-flat baseline shows that the form factor of the particles scales as q^{-2}. This dependence confirms the two-dimensional structure of the scatterers.

The distance between stacked neighbouring particles, corresponding to a pseudo-smectic period, is deduced from the present SAXS measurements. This distance is given by $d = 2\pi/q^*$ and is related to the thickness δ of the layer by the relationship $\phi_v = \delta/d$, where ϕ_v is the material volume fraction. This linear relationship holds only if the flakes repel each other so that they fill the whole volume of the sample. If this condition is satisfied, measurements of q^* as a function of ϕ allow the determination of δ. A linear dependence of ϕ_v as a function *of* $1/d$ is actually observed in figure 5*b* for both GO and RGO-BS. The volume fraction ϕ_v was deduced from the known weight fractions of the flakes and by assuming a density of $1.8\,g\,cm^{-3}$ for the materials. It is found from the slopes of linear fits in figure 5*b* that the thicknesses of GO and RGO-BS layers are, respectively, 0.55 nm and 0.60 nm. These results are in good agreement with previous measurements of the thickness of GO materials, thereby confirming single layer exfoliation in bulk. If the material were composed of a few layers of particles with a polydisperse distribution of thicknesses, it would not form liquid crystals with a regular spacing as evidenced by SAXS. Further analysis by AFM or TEM could be useful to obtain pictures of individual flakes but could not provide bulk characterizations. The present observation of thick RGO flakes is explained by considering remaining functional groups and surfactant molecules at their surface.

The above results show that the GO and RGO particles have similar lateral dimensions (assuming a circular shape for the flakes), thereby confirming the absence of chemical degradation during the chemical reduction. The average diameter D is estimated from the thickness of approximately 0.6 nm deduced from SAXS experiments divided by the aspect ratio of approximately 1.5×10^{-3} deduced from the phase behaviour. This approach yields $D \sim 400$ nm.

Nevertheless, in spite of their similar structural and phase behaviour, GO and RGO exhibit very different properties. A remarkable difference can be evidenced by investigating dry films made of GO or RGO-BS liquid crystals. Conductive thin films made from nematic liquid crystals of GO and RGO-BS are obtained by depositing a drop of nematic suspension onto a glass substrate and shearing it in a single direction with a second glass slide on top of it. Thus, macroscopic areas of about $2 \times 3\,cm^2$ are covered by graphene liquid crystals. The upper slide is removed so that water evaporates to achieve dried and oriented dried thin films. The thicknesses of the films, as measured by AFM and surface profilometry, are about 200 nm. GO films exhibit a surface resistivity of $500 \pm 100\,M\Omega$ per square. Similar films made from RGO-BS liquid crystals exhibit a surface resistivity of $0.7 \pm 0.2\,M\Omega$ per square, which differs by almost four orders of magnitude when compared with GO materials. These properties can generate significant interest in the use of RGO-BS liquid crystals for potential applications in electronic inks, sensors, electrodes, conductive coatings, etc.

4. Conclusion and new perspectives

The processing of CNTs and graphene particles as liquid crystals is certainly a promising approach towards the optimized manifestation of their physical properties in a number of applications. Challenges are still faced to fully exploit such liquid crystals, but several methods and successes have already been achieved at the laboratory scale. The phase behaviour of these liquid crystals is in good agreement with well-established theories. The ordering is controlled by the competition between translational and rotational entropy according to Onsager's theory [43]. It could thus be concluded that CNTs and graphene will not necessarily provide significant new knowledge in the field of liquid crystals in spite of their high aspect ratio and remarkable physical properties.

However, the liquid crystalline behaviour of such nanocarbons offers an indirect but valuable approach to obtain critical information on the investigated nanocarbons. First of all, the simple phase boundaries of a phase diagram provide information on the aspect ratio of the particles.

The width of the isotropic–nematic coexistence region reflects also the polydispersity of the materials. It is difficult to assess reliable and statistical information on such features using imaging techniques such as electron microscopy or atomic force microscopy. Phase diagrams of complex formulations as often used in applications such as electronic inks and bases for biomaterials can also provide information on the interaction between the particles. This was demonstrated, for example, for CNT liquid crystals stabilized in the presence of biomolecules such as DNA [23,59] or hyaluronic acid [25]. The different phase behaviours reflected the adsorbing character of DNA and the non-adsorbing character of hyaluronic acid, resulting in depletion of attractive interactions in the latter case. The phase behaviour of surfactant-stabilized RGO reflects repulsive electrostatic interactions provided by the surfactant molecules adsorbed at the interface of the particles. Lastly the phase behaviour associated with bulk structural characterizations such as those achieved by scattering techniques can provide additional information. Indeed, the average length or diameter of CNTs or graphene particles can be deduced from such characterizations as long as the aspect ratio has been determined from the phase behaviour.

These data are critical to compare different samples, and to understand and optimize their fundamental properties. From a more technological point of view, these data are also critical for future normalization and standardization of nanocarbon dispersions. Without such characterizations, most commercial developments will remain elusive. The liquid crystallinity of nanocarbons appears, therefore, as a valuable tool that can contribute to the standardization of nanocarbons. So far, little has been done in this direction. But it is certainly a promising route for further explorations. We have considered in this work basic thermodynamic and structural properties of liquid crystals. But there is still much more to explore if one considers the effect of fluctuations or dynamical and rheological properties. It is possible that future studies in the field could provide even more information, for example, on the persistence length of the particles and on their stiffness. This information is critical in applications in which mechanical properties are important. In conclusion, even if nanocarbons will perhaps not lead to a lot of new knowledge in the field of liquid crystals, there is no doubt that liquid crystals can teach us much about novel forms of nanocarbons.

References

1. Camponeschi E, Vance R, Al-Haik M, Garmestani H, Tannenbaum R. 2007 Properties of carbon nanotube–polymer composites aligned in a magnetic field. *Carbon* **45**, 2037–2046. (doi:10.1016/j.carbon.2007.05.024)
2. Choi ES, Brooks JS, Eaton DL, Al-Haik MS, Hussaini MY, Garmestani H, Li D, Dahmen K. 2003 Enhancement of thermal and electrical properties of carbon nanotube polymer composites by magnetic field processing. *J. Appl. Phys.* **94**, 6034–6039. (doi:10.1063/1.1616638)
3. Kordas K *et al.* 2007 Magnetic-field induced efficient alignment of carbon nanotubes in aqueous solutions. *Chem. Mater.* **19**, 787–791. (doi:10.1021/cm062196t)
4. Hone J, Llaguno MC, Nemes NM, Johnson AT, Fischer JE, Walters DA, Casavant MJ, Schmidt J, Smalley RE. 2000 Electrical and thermal transport properties of magnetically aligned single wall carbon nanotube films. *Appl. Phys. Lett.* **77**, 666–668. (doi:10.1063/1.127079)
5. Behabtu N, Green MJ, Pasquali M. 2008 Carbon nanotube-based neat fibers. *Nano Today* **3**, 24–34. (doi:10.1016/S1748-0132(08)70062-8)
6. Vigolo B, Penicaud A, Coulon C, Sauder C, Pailler R, Journet C, Bernier P, Poulin P. 2000 Macroscopic fibers and ribbons of oriented carbon nanotubes. *Science* **290**, 1331–1334. (doi:10.1126/science.290.5495.1331)
7. Ericson LM *et al.* 2004 Macroscopic, neat, single-walled carbon nanotube fibers. *Science* **305**, 1447–1450. (doi:10.1126/science.1101398)
8. Miaudet P, Badaire S, Maugey M, Derre A, Pichot V, Launois P, Poulin P, Zakri C. 2005 Hot-drawing of single and multiwall carbon nanotube fibers for high toughness and alignment. *Nano Lett.* **5**, 2212–2215. (doi:10.1021/nl051419w)
9. Li YL, Kinloch IA, Windle AH. 2004 Direct spinning of carbon nanotube fibers from chemical vapor deposition synthesis. *Science* **304**, 276–278. (doi:10.1126/science.1094982)
10. Zhang XF *et al.* 2007 Ultrastrong, stiff, and lightweight carbon-nanotube fibers. *Adv. Mater.* **19**, 4198–4201. (doi:10.1002/adma.200700776)

11. Scalia G. 2010 Alignment of carbon nanotubes in thermotropic and lyotropic liquid crystals. *ChemPhysChem* **11**, 333–340. (doi:10.1002/cphc.200900747)
12. Lynch MD, Patrick DL. 2002 Organizing carbon nanotubes with liquid crystals. *Nano Lett.* **2**, 1197–1201. (doi:10.1021/nl025694j)
13. Shah HJ, Fontecchio AK, Mattia D, Gogotsi Y. 2008 Field controlled nematic-to-isotropic phase transition in liquid crystal–carbon nanotube composites. *J. Appl. Phys.* **103**, 064314. (doi:10.1063/1.2844384)
14. Weiss V, Thiruvengadathan R, Regev O. 2006 Preparation and characterization of a carbon nanotube–lyotropic liquid crystal composite. *Langmuir* **22**, 854–856. (doi:10.1021/la052746m)
15. van der Schoot P, Popa-Nita V, Kralj S. 2008 Alignment of carbon nanotubes in nematic liquid crystals. *J. Phys. Chem. B* **112**, 4512–4518. (doi:10.1021/jp712173n)
16. Lagerwall JPF, Scalia G. 2008 Carbon nanotubes in liquid crystals. *J. Mater. Chem.* **18**, 2890–2898. (doi:10.1039/b802707b)
17. Lagerwall J, Scalia G, Haluska M, Dettlaff-Weglikowska U, Roth S, Giesselmann F. 2007 Nanotube alignment using lyotropic liquid crystals. *Adv. Mater.* **19**, 359–364. (doi:10.1002/adma.200600889)
18. Dierking I, Scalia G, Morales P. 2005 Liquid crystal–carbon nanotube dispersions. *J. Appl. Phys.* **97**, 044309. (doi:10.1063/1.1850606)
19. Schymura S *et al.* 2010 Towards efficient dispersion of carbon nanotubes in thermotropic liquid crystals. *Adv. Funct. Mater.* **20**, 3350–3357. (doi:10.1002/adfm.201000539)
20. Zhang SJ, Kumar S. 2008 Carbon nanotubes as liquid crystals. *Small* **4**, 1270–1283. (doi:10.1002/smll.200700082)
21. Song WH, Kinloch IA, Windle AH. 2003 Nematic liquid crystallinity of multiwall carbon nanotubes. *Science* **302**, 1363. (doi:10.1126/science.1089764)
22. Zakri C, Poulin P. 2006 Phase behavior of nanotube suspensions: from attraction induced percolation to liquid crystalline phases. *J. Mater. Chem.* **16**, 4095–4098. (doi:10.1039/b607378f)
23. Badaire S, Zakri C, Maugey M, Derre A, Barisci JN, Wallace G, Poulin P. 2005 Liquid crystals of DNA-stabilized carbon nanotubes. *Adv. Mater.* **17**, 1673–1676. (doi:10.1002/adma.200401741)
24. Islam MF, Alsayed AM, Dogic Z, Zhang J, Lubensky TC, Yodh AG. 2004 Nematic nanotube gels. *Phys. Rev. Lett.* **92**, 088303. (doi:10.1103/PhysRevLett.92.088303)
25. Moulton SE, Maugey M, Poulin P, Wallace GG. 2007 Liquid crystal behavior of single-walled carbon nanotubes dispersed in biological hyaluronic acid solutions. *J. Am. Chem. Soc.* **129**, 9452–9457. (doi:10.1021/ja072160h)
26. Rai PK, Pinnick RA, Parra-Vasquez ANG, Davis VA, Schmidt HK, Hauge RH, Smalley RE, Pasquali M. 2006 Isotropic–nematic phase transition of single-walled carbon nanotubes in strong acids. *J. Am. Chem. Soc.* **128**, 591–595. (doi:10.1021/ja055847f)
27. Lu LH, Chen W. 2010 Large-scale aligned carbon nanotubes from their purified, highly concentrated suspension. *ACS Nano* **4**, 1042–1048. (doi:10.1021/nn901326m)
28. Zamora-Ledezma C, Blanc C, Maugey M, Zakri C, Poulin P, Anglaret E. 2008 Anisotropic thin films of single-wall carbon nanotubes from aligned lyotropic nematic suspensions. *Nano Lett.* **8**, 4103–4107. (doi:10.1021/nl801525x)
29. Song WH, Windle AH. 2005 Isotropic–nematic phase transition of dispersions of multiwall carbon nanotubes. *Macromolecules* **38**, 6181–6188. (doi:10.1021/ma047691u)
30. Zhang SJ, Kinloch IA, Windle AH. 2006 Mesogenicity drives fractionation in lyotropic aqueous suspensions of multiwall carbon nanotubes. *Nano Lett.* **6**, 568–572. (doi:10.1021/nl0521322)
31. Song WH, Windle AH. 2008 Size-dependence and elasticity of liquid-crystalline multiwalled carbon nanotubes. *Adv. Mater.* **20**, 3149–3154. (doi:10.1002/adma.200702972)
32. Davis VA *et al.* 2009 True solutions of single-walled carbon nanotubes for assembly into macroscopic materials. *Nat. Nanotechnol.* **4**, 830–834. (doi:10.1038/nnano.2009.302)
33. Puech N, Blanc C, Grelet E, Zamora-Ledezma C, Maugey M, Zakri C, Anglaret E, Poulin P. 2011 Highly ordered carbon nanotube nematic liquid crystals. *J. Phys. Chem. C* **115**, 3272–3278. (doi:10.1021/jp1102077)
34. Puech N, Grelet E, Poulin P, Blanc C, van der Schoot P. 2010 Nematic droplets in aqueous dispersions of carbon nanotubes. *Phys. Rev. E* **82**, 020702. (doi:10.1103/PhysRevE.82.020702)
35. Zamora-Ledezma C, Blanc C, Puech N, Maugey M, Zakri C, Anglaret E, Poulin P. 2012 Publisher's note: Conductivity anisotropy of assembled and oriented carbon nanotubes [Phys. Rev. E 84, 062701 (2011)]. *Phys. Rev. E* **85**, 019901. (doi:10.1103/PhysRevE.85.019901)

36. Behabtu N *et al.* 2010 Spontaneous high-concentration dispersions and liquid crystals of graphene. *Nat. Nanotechnol.* **5**, 406–411. (doi:10.1038/nnano.2010.86)
37. Dan B, Behabtu N, Martinez A, Evans JS, Kosynkin DV, Tour JM, Pasquali M, Smalyukh II. 2011 Liquid crystals of aqueous, giant graphene oxide flakes. *Soft Matter* **7**, 11 154–11 159. (doi:10.1039/c1sm06418e)
38. Kim JE, Han TH, Lee SH, Kim JY, Ahn CW, Yun JM, Kim SO. 2011 Graphene oxide liquid crystals. *Angew. Chem. Int. Edn.* **50**, 3043–3047. (doi:10.1002/anie.201004692)
39. Xu Z, Gao C. 2011 Aqueous liquid crystals of graphene oxide. *ACS Nano* **5**, 2908–2915. (doi:10.1021/nn200069w)
40. Gudarzi MM, Zheng QB, Kim J-K. 2011 Spontaneous formation of liquid crystals in ultralarge graphene oxide dispersions. *Adv. Funct. Mater.* **21**, 2978–2988. (doi:10.1002/adfm.201100448)
41. Zamora-Ledezma C *et al.* 2012 Liquid crystallinity and dimensions of surfactant-stabilized sheets of reduced graphene oxide. *J. Phys. Chem. Lett.* **3**, 2425–2430. (doi:10.1021/jz3008479)
42. Hummers W, Offeman R. 1958 Preparation of graphitic oxide. *J. Am. Chem. Soc.* **80**, 1339. (doi:10.1021/ja01539a017)
43. Onsager L. 1949 The effects of shape on the interaction of colloidal particles. *Ann. NY Acad. Sci.* **51**, 627–659. (doi:10.1111/j.1749-6632.1949.tb27296.x)
44. Badaire S, Poulin P, Maugey M, Zakri C. 2004 In situ measurements of nanotube dimensions in suspensions by depolarized dynamic light scattering. *Langmuir* **20**, 10 367–10 370. (doi:10.1021/la049096r)
45. Lucas A, Zakri C, Maugey M, Pasquali M, van der Schoot P, Poulin P. 2009 Kinetics of nanotube and microfiber scission under sonication. *J. Phys. Chem. C* **113**, 20 599–20 605. (doi:10.1021/jp906296y)
46. Pagani G, Green MJ, Poulin P, Pasquali M. 2012 Competing mechanisms and scaling laws for carbon nanotube scission by ultrasonication. *Proc. Natl Acad. Sci. USA* **109**, 11 599–11 604. (doi:10.1073/pnas.1200013109)
47. Wenseleers W, Vlasov II, Goovaerts E, Obraztsova ED, Lobach AS, Bouwen A. 2004 Efficient isolation and solubilization of pristine single-walled nanotubes in bile salt micelles. *Adv. Funct. Mater.* **14**, 1105–1112. (doi:10.1002/adfm.200400130)
48. Fagan JA, Becker ML, Chun J, Hobbie EK. 2008 Length fractionation of carbon nanotubes using centrifugation. *Adv. Mater.* **20**, 1609–1613. (doi:10.1002/adma.200702353)
49. Grosberg A, Khokhlov A. 1981 Statistical theory of polymeric lyotropic liquid crystals. *Adv. Polym. Sci.* **41**, 53. (doi:10.1007/3-540-10554-9_10)
50. Prinsen P, van der Schoot P. 2003 Shape and director-field transformation of tactoids. *Phys. Rev. E* **68**, 021701. (doi:10.1103/PhysRevE.68.021701)
51. Fischer JE, Zhou W, Vavro J, Llaguno MC, Guthy C, Haggenmueller R, Casavant MJ, Walters DE, Smalley RE. 2003 Magnetically aligned single wall carbon nanotube films: preferred orientation and anisotropic transport properties. *J. Appl. Phys.* **93**, 2157–2163. (doi:10.1063/1.1536733)
52. Hecht D, Hu LB, Gruner G. 2006 Conductivity scaling with bundle length and diameter in single walled carbon nanotube networks. *Appl. Phys. Lett.* **89**, 133112. (doi:10.1063/1.2356999)
53. Fuhrer MS *et al.* 2000 Crossed nanotube junctions. *Science* **288**, 494–497. (doi:10.1126/science.288.5465.494)
54. Li SD, Yu Z, Rutherglen C, Burke PJ. 2004 Electrical properties of 0.4 cm long single-walled carbon nanotubes. *Nano Lett.* **4**, 2003–2007. (doi:10.1021/nl048687z)
55. Li D, Muller MB, Gilje S, Kaner RB, Wallace GG. 2008 Processable aqueous dispersions of graphene nanosheets. *Nat. Nanotechnol.* **3**, 101–105. (doi:10.1038/nnano.2007.451)
56. Dikin DA, Stankovich S, Zimney EJ, Piner RD, Dommett GHB, Evmenenko G, Nguyen ST, Ruoff RS. 2007 Preparation and characterization of graphene oxide paper. *Nature* **448**, 457–460. (doi:10.1038/nature06016)
57. van der Kooij FM, Lekkerkerker HNW. 1998 Formation of nematic liquid crystals in suspensions of hard colloidal platelets. *J. Phys. Chem. B* **102**, 7829–7832. (doi:10.1021/jp981534d)
58. Veerman JAC, Frenkel D. 1992 Phase-behavior of disk-like hard-core mesogens. *Phys. Rev. A* **45**, 5632–5648. (doi:10.1103/PhysRevA.45.5632)
59. Tardani F, La Mesa C, Poulin P, Maugey M. 2012 Phase behavior of DNA-based dispersions containing carbon nanotubes: effects of added polymers and ionic strength on excluded volume. *J. Phys. Chem. C* **116**, 9888–9894. (doi:10.1021/jp300691w)